J|A|C|S
ARTICLES
Published on Web 04/24/2007

Spectroscopic and Computational Evaluation of the Structure of the High-Spin Fe(IV)-Oxo Intermediates in Taurine: α-Ketoglutarate Dioxygenase from *Escherichia coli* and Its His99Ala Ligand Variant

Sebastian Sinnecker,[†] Nina Svensen,[‡] Eric W. Barr,[‡] Shengfa Ye,[†,§] J. Martin Bollinger, Jr.,*[,‡,||] Frank Neese,*[,†,§] and Carsten Krebs*[,‡,||]

Contribution from the Max-Planck Institut für Bioanorganische Chemie, D-45470 Mülheim an der Ruhr, Germany, Department of Biochemistry and Molecular Biology, The Pennsylvania State University, University Park, Pennsylvania 16802, Institut für Physikalische und Theoretische Chemie, Universität Bonn, D-53115 Bonn, Germany, and Department of Chemistry, The Pennsylvania State University, University Park, Pennsylvania 16802

Received November 9, 2006; E-mail: jmb21@psu.edu; neese@thch.uni-bonn.de; ckrebs@psu.edu

Abstract: The Fe(II)- and α-ketoglutarate (αKG)-dependent dioxygenases activate O_2 for cleavage of unactivated C−H bonds in their substrates. The key intermediate that abstracts hydrogen in the reaction of taurine:αKG dioxygenase (TauD), a member of this enzyme family, was recently characterized. The intermediate, denoted **J**, was shown to contain an iron(IV)-oxo unit. Other important structural features of **J**, such as the number, identity, and disposition of ligands in the Fe(IV) coordination sphere, are not yet understood. To probe these important structural features, a series of models for **J** with the Fe(IV) ion coordinated by the expected two imidazole (from His99 and His255), two carboxylate (succinate and Asp101), and oxo ligands have been generated by density functional theory (DFT) calculations, and spectroscopic parameters (Mössbauer isomer shift, quadrupole splitting, and asymmetry parameter, ^{57}Fe hyperfine coupling tensor, and zero field splitting parameters, *D* and *E*/*D*) have been calculated for each model. The calculated parameters of distorted octahedral models for **J**, in which one of the carboxylates serves as a monodentate ligand and the other as a bidentate ligand, and a trigonal bipyramidal model, in which both carboxylates serve as monodentate ligands, agree well with the experimental parameters, whereas the calculated parameters of a square pyramidal model, in which the oxo ligand is in the equatorial plane, are inconsistent with the data. Similar analysis of the Fe(IV) complex generated in the variant protein with His99, the residue that contributes the imidazole ligand *cis* to the oxo group, replaced by alanine suggests that the deleted imidazole is replaced by a water ligand. This work lends credence to the idea that the combination of Mössbauer spectroscopy and DFT calculations can provide detailed structural information for reactive intermediates in the catalytic cycles of iron enzymes.

Introduction

The Fe(II)- and α-ketoglutarate-dependent oxygenases are a large family of enzymes[1−4] that catalyze steps in, among other processes, the biosyntheses of antibiotics[5] and collagen,[6,7] the repair of alkylated DNA,[8,9] the detection of and response to oxygen insufficiency (hypoxia),[10−17] and the regulation of gene expression.[18−20] They couple the reductive activation of dioxy-

[†] Max-Planck Institut für Bioanorganische Chemie.
[‡] Department of Biochemistry and Molecular Biology, The Pennsylvania State University.
[§] Universität Bonn.
[||] Department of Chemistry, The Pennsylvania State University.

(1) Solomon, E. I.; Brunold, T. C.; Davis, M. I.; Kemsley, J. N.; Lee, S.-K.; Lehnert, N.; Neese, F.; Skulan, A. J.; Yang, Y.-S.; Zhou, J. *Chem. Rev.* **2000**, *100*, 235−349.
(2) Costas, M.; Mehn, M. P.; Jensen, M. P.; Que, L., Jr. *Chem. Rev.* **2004**, *104*, 939−986.
(3) Hausinger, R. P. *Crit. Rev. Biochem. Mol. Biol.* **2004**, *39*, 21−68.
(4) Bollinger, J. M., Jr.; Price, J. C.; Hoffart, L. M.; Barr, E. W.; Krebs, C. *Eur. J. Inorg. Chem.* **2005**, *2005*, 4245−4254.
(5) Kershaw, N. J.; Caines, M. E. C.; Sleeman, M. C.; Schofield, C. J. *Chem. Comm.* **2005**, 4251−4263.
(6) Hutton, J. J., Jr.; Tappel, A. L.; Udenfriend, S. *Biochem. Biophys. Res. Commun.* **1966**, *24*, 179−184.
(7) Kivirikko, K. I.; Myllyharju, J. *Matrix Biol.* **1998**, *16*, 357−368.
(8) Trewick, S. C.; Henshaw, T. F.; Hausinger, R. P.; Lindahl, T.; Sedgwick, B. *Nature* **2002**, *419*, 174−178.
(9) Falnes, P. Ø.; Johansen, R. F.; Seeberg, E. *Nature* **2002**, *419*, 178−182.
(10) Ivan, M.; Kondo, K.; Yang, H.; Kim, W.; Valiando, J.; Ohh, M.; Salic, A.; Asara, J. M.; Lane, W. S.; Kaelin, W. G., Jr. *Science* **2001**, *292*, 464−468.
(11) Jaakkola, P.; Mole, D. R.; Tian, Y.-M.; Wilson, M. I.; Gielbert, J.; Gaskell, S. J.; von Kriegsheim, A.; Hebestreit, H. F.; Mukherji, M.; Schofield, C. J.; Maxwell, P. H.; Pugh, C. W.; Ratcliffe, P. J. *Science* **2001**, *292*, 468−472.
(12) Epstein, A. C. R. et al. *Cell* **2001**, *107*, 43−54.
(13) Bruick, R. K.; McKnight, S. L. *Science* **2001**, *294*, 1337−1340.
(14) Yu, F.; White, S. B.; Zhao, Q.; Lee, F. S. *Proc. Natl. Acad. Sci. U.S.A.* **2001**, *98*, 9630−9635.
(15) Masson, N.; Willam, C.; Maxwell, P. H.; Pugh, C. W.; Ratcliffe, P. J. *EMBO J.* **2001**, *20*, 5197−5206.
(16) Lando, D.; Peet, D. J.; Whelan, D. A.; Gorman, J. J.; Whitelaw, M. L. *Science* **2002**, *295*, 858−861.
(17) Hewitson, K. S.; McNeill, L. A.; Riordan, M. V.; Tian, Y.-M.; Bullock, A. N.; Welford, R. W.; Elkins, J. M.; Oldham, N. J.; Bhattacharya, S.; Gleadle, J. M.; Ratcliffe, P. J.; Pugh, C. W.; Schofield, C. J. *J. Biol. Chem.* **2002**, *277*, 26351−26355.
(18) Tsukada, Y.-i.; Fang, J.; Erdjument-Bromage, H.; Warren, M. E.; Borchers, C. H.; Tempst, P.; Zhang, Y. *Nature* **2006**, *439*, 811−816.

 10.1021/ja067899q CCC: $37.00

Scheme 1. Proposed Mechanism of the Fe(II)- and α-Ketoglutarate-Dependent Dioxygenases

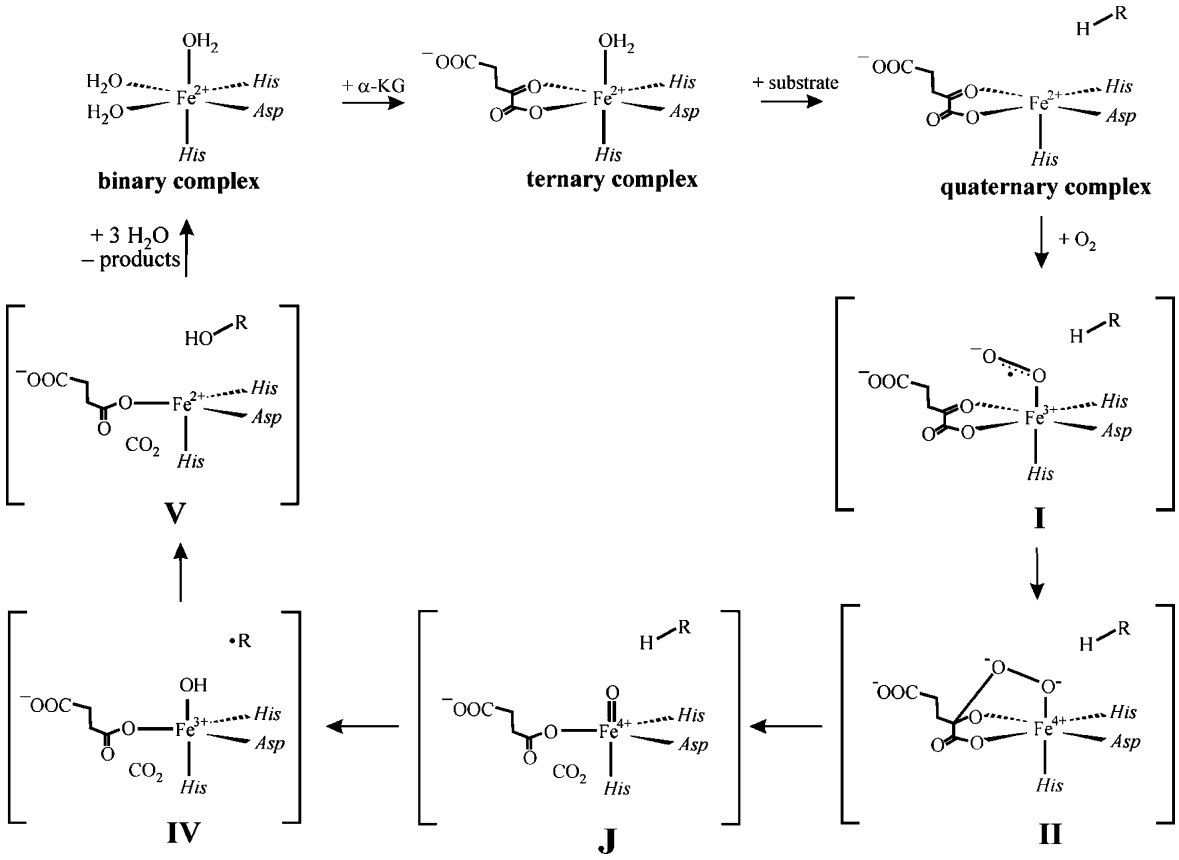

gen to the oxidation of their substrates and the decarboxylation of the cosubstrate, α-ketoglutarate (αKG), to succinate. In most of the reactions, the substrate is hydroxylated, but other outcomes, including desaturation, cyclization, and halogenation, also occur.[1−3,21,22] In each case, the reaction is carried out at a mononuclear non-heme Fe center, which (with the exception of the absence of the carboxylate ligand in the halogenases) is always facially coordinated by a conserved $(His)_2$-(Asp/Glu) motif.[23,24]

It is believed that these enzymes follow a conserved chemical mechanism, which was formulated more than 20 years ago by Hanauske-Abel and Günzler[25] (see Scheme 1).[1−4] Although this mechanism had been supported by a large number of experimental studies (see refs 1−3 and references cited therein), prior to 2003 none of the proposed intermediates following the addition of oxygen had been directly detected. Recent investigations of taurine:α-ketoglutarate dioxygenase (TauD) led to the detection of two accumulating, kinetically competent intermediate states upon reaction of the TauD•Fe(II)•αKG•taurine complex with O_2.[26] A combination of Mössbauer and EPR spectroscopies revealed that the first intermediate, which was termed **J**, contains an Fe ion in the +IV oxidation state and the unusual high-spin ($S = 2$) configuration.[26] Demonstration of a large kinetic isotope effect on decay of **J** upon substitution of the H-atoms bonded to C1 of the substrate, taurine, with deuteria proved that **J** is the species that initiates C1 hydroxylation by abstracting hydrogen.[27] In the consensus mechanism, this species is an Fe(IV)-oxo (ferryl) complex. The presence of the ferryl unit in **J** was demonstrated by two independent spectroscopic studies. Using low-temperature continuous-flow resonance Raman spectroscopy, Proshlyakov et al. detected a band at 821 cm^{-1} that downshifted to 787 cm^{-1} upon use of $^{18}O_2$.[28] Subsequently, freeze-quench X-ray absorption spectroscopy was used to demonstrate that **J** exhibits a short (1.62 Å) iron−ligand interaction, which was attributed to the oxo ligand.[29] Whereas the results provided definitive proof for the presence of the ferryl unit in **J**, they could not reveal other important structural features, such as the number, identity, and disposition of ligands in the Fe(IV) coordination sphere.

Almost all ferryl complexes studied prior to **J**, including heme-enzyme intermediates, synthetic models thereof (see ref 30 and references cited therein), and synthetic non-heme ferryl complexes,[31−34] have $S = 1$ electronic ground states. Only the

(19) Cloos, P. A. C.; Christensen, J.; Agger, K.; Maiolica, A.; Rappsilber, J.; Antal, T.; Hansen, K. H.; Helin, K. *Nature* **2006**, *442*, 307−311.
(20) Klose, R. J.; Yamane, K.; Bae, Y.; Zhang, D.; Erdjument-Bromage, H.; Tempst, P.; Wong, J.; Zhang, Y. *Nature* **2006**, *442*, 312−316.
(21) Vaillancourt, F. H.; Yin, J.; Walsh, C. T. *Proc. Natl. Acad. Sci. U.S.A.* **2005**, *102*, 10111−10116.
(22) Blasiak, L. C.; Vaillancourt, F. H.; Walsh, C. T.; Drennan, C. L. *Nature* **2006**, *440*, 368−371.
(23) Que, L., Jr. *Nat. Struct. Biol.* **2000**, *7*, 182−184.
(24) Koehntop, K. D.; Emerson, J. P.; Que, L., Jr. *J. Biol. Inorg. Chem.* **2005**, *10*, 87−93.
(25) Hanauske-Abel, H. M.; Günzler, V. *J. Theor. Biol.* **1982**, *94*, 421−455.
(26) Price, J. C.; Barr, E. W.; Tirupati, B.; Bollinger, J. M., Jr.; Krebs, C. *Biochemistry* **2003**, *42*, 7497−7508.
(27) Price, J. C.; Barr, E. W.; Glass, T. E.; Krebs, C.; Bollinger, J. M., Jr. *J. Am. Chem. Soc.* **2003**, *125*, 13008−13009.
(28) Proshlyakov, D. A.; Henshaw, T. F.; Monterosso, G. R.; Ryle, M. J.; Hausinger, R. P. *J. Am. Chem. Soc.* **2004**, *126*, 1022−1023.
(29) Riggs-Gelasco, P. J.; Price, J. C.; Guyer, R. B.; Brehm, J. H.; Barr, E. W.; Bollinger, J. M., Jr.; Krebs, C. *J. Am. Chem. Soc.* **2004**, *126*, 8108−8109.
(30) Debrunner, P. G. *Phys. Bioinorg. Chem. Ser.* **1989**, *4*, 137−234.
(31) Grapperhaus, C. A.; Mienert, B.; Bill, E.; Weyhermüller, T.; Wieghardt, K. *Inorg. Chem.* **2000**, *39*, 5306−5317.
(32) Rohde, J.-U.; In, J.-H.; Lim, M. H.; Brennessel, W. W.; Bukowski, M. R.; Stubna, A.; Münck, E.; Nam, W.; Que, L., Jr. *Science* **2003**, *299*, 1037−1039.

$[Fe(IV)(O)(H_2O)_5]^{2+}$ complex reported by Pestovsky et al.[35] and a dinuclear complex reported by Zheng et al.[36] have the high-spin configuration. Subsequent to the discovery of **J**, high-spin Fe(IV) intermediates that exhibit similar spectroscopic parameters and presumably also contain the ferryl unit have been detected in two other Fe(II)- and αKG-dependent oxygenases, prolyl-4-hydroxylase[37] and the halogenase CytC3.[38] The unusual $S = 2$ ground state of **J** was previously rationalized by density functional theory (DFT) calculations on a model with trigonal bipyramidal geometry.[39] This geometry was chosen because, in a trigonal bipyramidal ligand field, the d-orbitals split into a high-energy a_1 orbital and two sets of lower-lying *e* orbitals. The *e* orbitals could accommodate four unpaired electrons, resulting in the experimentally observed $S = 2$ ground state. More recently, experimental and theoretical studies on the octahedral $[Fe(IV)(O)(H_2O)_5]^{2+}$ complex[35] and computational studies on the hypothetical, octahedral $[Fe(IV)(O)(NH_3)_5]^{2+}$ complex[40] demonstrated that the high-spin ground state can also be stabilized in an octahedral ligand field, provided that the ligands in the *xy*-plane are weak donors (the $Fe-O_{oxo}$ bond defines the *z*-axis).

Recent developments have made it possible to calculate electronic structure parameters (e.g., Mössbauer isomer shift, δ; Mössbauer quadrupole splitting parameter, ΔE_Q; Mössbauer asymmetry parameter, η; ^{57}Fe hyperfine coupling tensor, **A**; zero-field splitting parameter, *D*; rhombicity, *E*/*D*; and g-tensor, **g**) for structural models of iron complexes derived by DFT.[35,41−47] Very recently, the approach of comparing parameters calculated for a series of DFT-derived models to the experimentally measured values was used to provide insight into the structure of the diiron(III/IV) intermediate **X** from *E. coli* class I ribonucleotide reductase.[48−50] In this work, we have used this approach to define the geometric structure of **J** in greater detail. By including a similar analysis of the spectroscopically distinct Fe(IV) intermediate that forms in a variant of TauD with the His99 ligand replaced by alanine, we have added a third dimension (perturbation by mutagenesis) to the combined computational/spectroscopic approach to defining the structures of fleeting intermediates in the reactions of iron enzymes.

Materials and Methods

Construction of His99Ala-TauD Overexpression Strain. The genetic change specifying the His99Ala substitution was introduced by PCR amplification of the *tauD* gene in two fragments. The previously described plasmid containing the wild-type *tauD* gene in pET22b was used as the template.[26] Primers 1 (5′-GGAGAAGTCATATGAGTGAACG-3′) and 2 (5′-GCCCCGGCCGGTGGCGTTTCAATAAATGTCACATCGGT**AGC**CCAGTTGTCG-3′) amplified a 348 base-pair fragment encoding the N-terminus of TauD, with primer 1 containing an ***Nde***I site (underlined) for ligation with pET22b and primer 2 specifying both the desired amino acid substitution (complement of bolded triplet) and new, unique *Eag*I restriction site (underlined) for internal ligation. Primers 3 (5′-CGACAACTGG**GCT**ACCGATGTGACATTTATTGAAACGCCACCGGCCGGGGC-3′) and 4 (5′-CCGTCCACTCTCGAGTTACCCC-3′) amplified a 586 base-pair fragment encoding the C-terminus of TauD, with primer 3 encoding the desired substitution (bolded triplet) and *Eag*I site for internal ligation (underlined) and primer 4 containing a unique *Xho*I site (underlined) for ligation with pET22b. The two PCR fragments were purified by agarose gel electrophoresis, restricted with *Eag*I, and ligated. The ligation mixture was used as a template for PCR amplification of the entire variant gene with primers 1 and 4. The resulting 880 base-pair fragment was restricted with *Nde*I and *Xho*I and ligated with vector (pET22b) that had been restricted with the same two enzymes. The ligation solution was used to transform *E. coli* DH5α to ampicillin resistance. The entire coding sequence was verified. The plasmid was then used to transform the expression strain, *E. coli* BL21(DE3).

Protein Expression and Purification: Wild-type (wt) and His99Ala-TauD were expressed and purified as previously described.[26]

Sample Preparation: Samples suitable for Mössbauer spectroscopy were prepared by the freeze-quench method, as previously described.[26] Experimental conditions are given in the figure legends.

Spectroscopic Experiments: The spectrometers have been described.[26] Analysis of the Mössbauer data was performed with the program WMOSS (Web Research, Edina, MN). The simulations are based on the following spin Hamiltonian, in which the first three terms describe the electron Zeeman effect and zero-field splitting of the $S = 2$ ground state, the fourth term represents the interaction between the electric field gradient and the nuclear quadrupole moment, the fifth term describes the magnetic hyperfine interactions between the electronic spin and the ^{57}Fe nucleus, and the last term represents the nuclear Zeeman interaction.

$$\mathbf{H} = \beta \mathbf{S}\cdot\mathbf{g}\cdot\mathbf{B} + D\left(\mathbf{S}_z^2 - \frac{S(S+1)}{3}\right) + E(\mathbf{S}_x^2 - \mathbf{S}_y^2) + \frac{eQV_{zz}}{12}[3\mathbf{I}_z^2 - I(I+1) + \eta(\mathbf{I}_x^2 - \mathbf{I}_y^2)] + \mathbf{S}\cdot\mathbf{A}\cdot\mathbf{I} - g_n\beta_n\mathbf{B}\cdot\mathbf{I} \quad (1)$$

Computational Details: All calculations were performed with the program package ORCA.[51]

Geometry Optimizations. Intermediate **J** was modeled as an iron-oxo complex coordinated by two methyl imidazole ligands and two carboxylate ligands. Several initial structures that differ in their metal−ligand distances, ligand conformations, and spin states were generated and completely geometry optimized with the BP86 density functional.[52−54] The TZVP[55] (Fe, O, and N) and SV(P) basis sets[56] (other elements) were applied, in combination with the auxiliary basis sets TZV/J (Fe, O, and N) and SV/J.[57,58] All basis functions were taken from the Turbomole basis set library.[59,60] The resolution of the identity (RI) approximation was used to accelerate the calculations.[57,61]

(33) Lim, M. H.; Rohde, J.-U.; Stubna, A.; Bukowski, M. R.; Costas, M.; Ho, R. Y. N.; Münck, E.; Nam, W.; Que, L., Jr. *Proc. Natl. Acad. Sci. U.S.A.* **2003**, *100*, 3665−3670.
(34) Bukowski, M. R.; Koehntop, K. D.; Stubna, A.; Bominaar, E. L.; Halfen, J. A.; Münck, E.; Nam, W.; Que, L., Jr. *Science* **2005**, *310*, 1000−1002.
(35) Pestovsky, O.; Stoian, S.; Bominaar, E. L.; Shan, X.; Münck, E.; Que, L., Jr.; Bakac, A. *Angew. Chem., Int. Ed.* **2005**, *44*, 6871−6874.
(36) Zheng, H.; Yoo, S. J.; Münck, E.; Que, L., Jr. *J. Am. Chem. Soc.* **2000**, *122*, 3789−3790.
(37) Hoffart, L. M.; Barr, E. W.; Guyer, R. B.; Bollinger, J. M., Jr.; Krebs, C. *Proc. Natl. Acad. Sci., U.S.A.* **2006**, *103*, 14738−14743.
(38) Galonić, D. P.; Barr, E. W.; Walsh, C. T.; Bollinger, J. M., Jr.; Krebs, C. *Nature Chem. Biol.* **2007**, *3*, 113−116.
(39) Krebs, C.; Price, J. C.; Baldwin, J.; Saleh, L.; Green, M. T.; Bollinger, J. M., Jr. *Inorg. Chem.* **2005**, *44*, 742−757.
(40) Neese, F. *J. Inorg. Biochem.* **2006**, *100*, 716−726.
(41) Neese, F. *Inorg. Chim. Acta* **2002**, *337*, 181−192.
(42) Neese, F. *Curr. Opin. Chem. Biol.* **2003**, *7*, 125−135.
(43) Sinnecker, S.; Slep, L. D.; Bill, E.; Neese, F. *Inorg. Chem.* **2005**, *44*, 2245−2254.
(44) Schöneboom, J. C.; Neese, F.; Thiel, W. *J. Am. Chem. Soc.* **2005**, *127*, 5840−5853.
(45) Zhang, Y.; Mao, J.; Oldfield, E. *J. Am. Chem. Soc.* **2002**, *124*, 7829−7839.
(46) Zhang, Y.; Oldfield, E. *J. Am. Chem. Soc.* **2004**, *126*, 4470−4471.
(47) Vrajmasu, V.; Münck, E.; Bominaar, E. L. *Inorg. Chem.* **2003**, *42*, 5974−5988.
(48) Liu, T.; Lovell, T.; Han, W.-G.; Noodleman, L. *Inorg. Chem.* **2003**, *42*, 5244−5251.
(49) Han, W.-G.; Liu, T.; Lovell, T.; Noodleman, L. *J. Am. Chem. Soc.* **2005**, *127*, 15778−15790.
(50) Han, W.-G.; Liu, T.; Lovell, T.; Noodleman, L. *J. Inorg. Biochem.* **2006**, *100*, 771−779.
(51) Neese, F. *ORCA - an ab initio, Density Functional and Semiempirical Program Package*, version 2.4; Mülheim an der Ruhr, Max-Planck Institut für Bioanorganische Chemie: 2004.

Spectroscopic Parameters. The spectroscopic data were obtained from additional single-point calculations. For that purpose, the B3LYP hybrid density functional[62,63] and the BP86 density functional (only for zero-field splitting parameters) were applied in combination with the CP(PPP) basis set for Fe[41] and the TZVP basis set for the N and O atoms. The justification for this mixed BP86/B3LYP approach has been presented.[64] The SV(P) basis sets were used for the remaining atoms.[56] The TZV/J (Fe, N, and O) and SV/J (H, C) auxiliary basis sets[57,61] from the Turbomole 5.3 basis set library were employed.[60]

Quadrupole splittings ΔE_Q were obtained from electric field gradients V_i ($i = x, y, z$) by employing a nuclear quadrupole moment, $Q(^{57}\text{Fe})$, of 0.16 barn:[43]

$$\Delta E_Q = \frac{1}{2} eQ \cdot V_z \cdot \sqrt{1 + \frac{1}{3}\eta^2} \tag{2}$$

Here, $\eta = (V_x - V_y)/V_z$ is the asymmetry parameter of the nuclear quadrupole tensor. Isomer shifts, δ, were calculated from the electron densities at the Fe nuclei, ρ_0, by employing the fit equation

$$\delta = \alpha \cdot (\rho_0 - C) + \beta \tag{3}$$

C is a constant of 11 800 au^{-3}, and $\alpha = -0.367$ au^3·mm/s and $\beta = +6.55$ mm/s are the fit parameters from our previous work.[43] It should be noted that these fit parameters strongly depend on the chosen functionals and basis sets. Here, the same approach was used as in our previous work. The magnetic hyperfine data were calculated by employing the scalar relativistic zero-order regular approximation (ZORA) in combination with the B3LYP functional.[65−67] The suitability of this approach for the calculation of accurate hyperfine data was demonstrated in recent studies.[68,69] In our implementation, Gaussian-type orbitals were used and a model potential derived from atomic ZORA calculations was applied, based on the work of van Wüllen.[70] Here, the magnetic hyperfine parameters $A_i/g_N\beta_N$ ($i = x, y, z$) of the ^{57}Fe center were calculated by taking into account the isotropic Fermi contact term, the first-order traceless dipolar contribution, and the second-order nontraceless spin−orbit contribution. The Fermi contact contributions were scaled by a factor of 1.69, according to our previous study.[43] Spin−orbit contributions to the hyperfine tensors were calculated as second-order properties by employing the coupled-perturbed (CP) Kohn−Sham theory.[71]

Due to the present limitations of the ZFS theory in a DFT framework, the ZFS parameters D and E/D were calculated in an approximation due to Pederson and Khanna[72] that employed the BP86 density functional and the following uncoupled equation for the SOC contribution to the zero-field splitting tensor:

$$D_{\mu\nu} = -\sum_{\sigma\sigma'=\alpha,\beta} \frac{(-1)^{\sigma+\sigma'}}{4S^2} \sum_{i\in\sigma} \sum_{a\in\sigma'} \frac{\langle \psi_i^{\sigma} | h_\mu^{SOC} | \psi_a^{\sigma'} \rangle \langle \psi_a^{\sigma'} | h_\nu^{SOC} | \psi_i^{\sigma} \rangle}{\epsilon_{a\sigma'} - \epsilon_{i\sigma}} \tag{4}$$

(For an alternative approach based on a different philosophy, see refs 44, 73, and 74). Here, S is the ground state spin, ψ_i^{σ} are the occupied MOs of spin $\sigma = \alpha, \beta$ with orbital energies $\epsilon_{i\sigma}$; $\psi_a^{\sigma'}$ are the virtual MOs of spin $\sigma' = \alpha, \beta$ with orbital energies $\epsilon_{a\sigma'}$. The operators h^{SOC} are the spatial parts of the effective one electron SOC operators calculated as described in ref 75. It was shown that a considerable underestimation of E must be expected from this approach, mainly due to the lack of accurate energy denominators and incorrect spin-flip prefactors in eq 4.[44] Although not listed explicitly, our calculations also included the spin−spin contribution to the ZFS (see refs 73 and 76) which is, however, less important in the present case due to the large SOC contribution.

Total energy calculations were performed with the B3LYP hybrid functional in combination with large basis sets for all elements (TZVP for hydrogen and TZVPP for all other elements; see;[55] exponents of polarization functions were taken from the TurboMole library[60]).

Results and Discussion

Computational Studies on Intermediate J from Wild-Type TauD. Complete geometry optimizations were performed for model systems containing the Fe(IV)-oxo moiety coordinated by two methyl imidazoles to mimic the two histidine ligands (His99 and His255) and two propionates to mimic the aspartate (Asp101) and succinate ligands (see structure **J** in Scheme 1). The succinate is formed by decarboxylation of the coordinated αKG during formation of **J**. Two possible spin states ($S = 2$ and $S = 1$) and several different coordination geometries were considered. A subset of the investigated structures is shown in Figure 1. The Mulliken spin populations and important geometrical parameters of the various model structures are compared in Table 1, and calculated spectroscopic parameters are compared to the experimentally measured values in Table 2.[77]

The structures differ mainly in the binding mode of the two carboxylate ligands. For the $S = 1$ structures, **6**−**8**, both carboxylate ligands are monodentate, with the uncoordinated O-atoms more than 3.4 Å away from the Fe. The binding modes of the two carboxylates vary from (*syn*, *anti*) in **6**, to (*anti*, *anti*) in **7**, to (*syn*, *syn*) in **8**. The coordination environment of **6**−**8** is best described as square pyramidal with the oxo ligand in the equatorial plane. In **9**, one of the carboxylate ligands is *anti*-monodentate, whereas the second carboxylate chelates the Fe-center almost symmetrically (difference between the two Fe−O bonds (Δ) of 0.02 Å), resulting in a distorted octahedral coordination environment.

Similar structural variability is observed for the high-spin models, **1**−**5**. Two of the structures with $S = 2$ ground state, **4** and **5**, have two monodentate carboxylate ligands in the (*syn*,

(52) Becke, A. D. *Phys. Rev. A*: *At., Mol., Opt. Phys.* **1988**, *38*, 3098−3100.
(53) Perdew, J. P. *Phys. Rev. B* **1986**, *34*, 7406.
(54) Perdew, J. P. *Phys. Rev. B* **1986**, *33*, 8822−8824.
(55) Schäfer, A.; Huber, C.; Ahlrichs, R. *J. Chem. Phys.* **1994**, *100*, 5829−5835.
(56) Schäfer, A.; Horn, H.; Ahlrichs, R. *J. Chem. Phys.* **1992**, *97*, 2571−2577.
(57) Eichkorn, K.; Weigend, F.; Treutler, O.; Ahlrichs, R. *Theor. Chem. Acc.* **1997**, *97*, 119−124.
(58) Eichkorn, K.; Treutler, O.; Öhm, H.; Häser, M.; Ahlrichs, R. *Chem. Phys. Lett.* **1995**, *240*, 283−290.
(59) Ahlrichs, R. et al. *Turbomole* (5.3); Quantum Chemistry Group, University of Karlsruhe: Karlsruhe, Germany, 2000.
(60) The basis sets can be downloaded from the ftp server of the Turbomole home page: http://www.turbomole.com.
(61) Eichkorn, K.; Treutler, O.; Öhm, H.; Häser, M.; Ahlrichs, R. *Chem. Phys. Lett.* **1995**, *242*, 652−660.
(62) Becke, A. D. *J. Chem. Phys.* **1993**, *98*, 5648−5652.
(63) Lee, C. T.; Yang, W. T.; Parr, R. G. *Phys. Rev. B* **1988**, *37*, 785−789.
(64) Neese, F. *J. Biol. Inorg. Chem.* **2006**, *11*, 702−711.
(65) van Lenthe, E.; Baerends, E. J.; Snijders, J. G. *J. Chem. Phys.* **1993**, *99*, 4597−4610.
(66) van Lenthe, E.; Baerends, E. J.; Snijders, J. G. *J. Chem. Phys.* **1994**, *101*, 9783−9792.
(67) van Lenthe, E.; van Leeuwen, R.; Baerends, E. J.; Snijders, J. G. *Int. J.Quantum Chem.* **1996**, *57*, 281−293.
(68) van Lenthe, E.; van der Avoird, A.; Wormer, P. E. S. *J. Chem. Phys.* **1998**, *108*, 4783−4796.
(69) Belanzoni, P.; van Lenthe, E.; Baerends, E. J. *J. Chem. Phys.* **2001**, *114*, 4421−4433.
(70) van Wüllen, C. *J. Chem. Phys.* **1998**, *109*, 392−399.
(71) Neese, F. *J. Chem. Phys.* **2003**, *118*, 3939−3948.
(72) Pederson, M. R.; Khanna, S. N. *Phys. Rev. B: Condens. Matter* **1999**, *60*, 9566−9572.
(73) Neese, F. *J. Am. Chem. Soc.* **2006**, *128*, 10213−10222.
(74) Ray, K.; Begum, A.; Weyhermüller, T.; Piligkos, S.; Van Slageren, J.; Neese, F.; Wieghardt, K. *J. Am. Chem. Soc.* **2005**, *127*, 4403−4415.
(75) Neese, F. *J. Chem. Phys.* **2005**, *122*, 034107.
(76) Sinnecker, S.; Neese, F. *J. Chem. Phys. A* **2006**, *110*, 12267−12275.
(77) The computed principal components of the **g**-tensor are similar to the free electron *g*-value, as was observed previously. The Mössbauer spectra are insensitive to moderate anisotropy of the **g**-tensor.

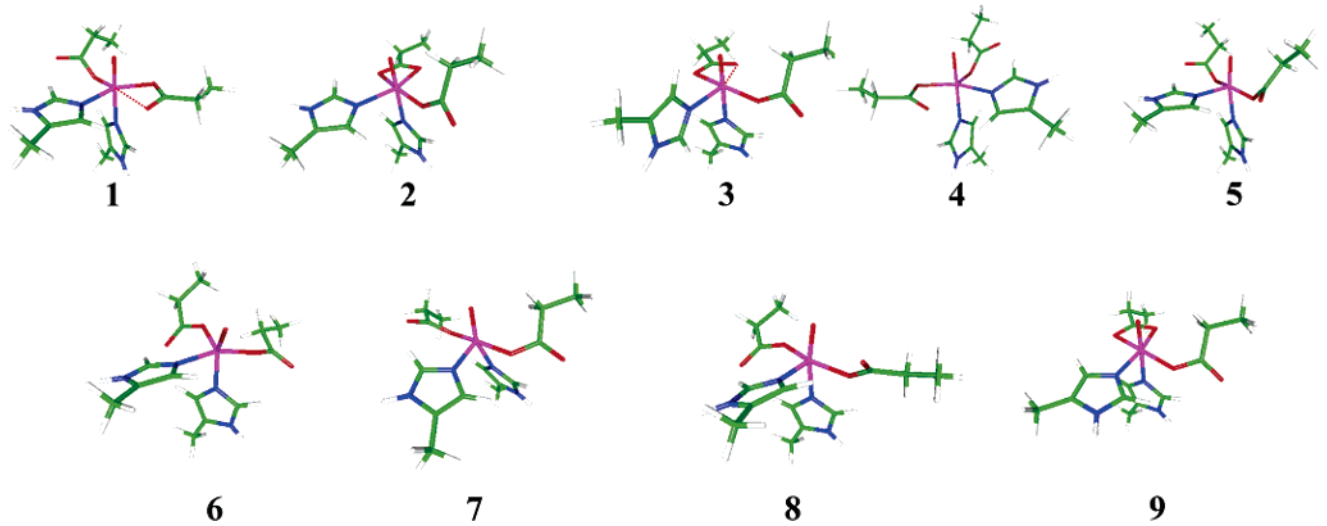

Figure 1. Geometry optimized models of intermediate **J** from wild-type TauD. Structures **1** through **5** are quintet states, and structures **6** through **9** are triplet states. Color code: iron (magenta), oxygen (red), nitrogen (blue), carbon (green), hydrogen (gray). The dotted lines in **1** and **3** represent the longer Fe−O bond of the chelating carboxylate ligand.

Table 1. Mulliken Spin Populations ρ and Geometrical Parameter of Structures **1**−**9** from Figure 1 as a Model for **J** from Wild-Type TauD[a]

	S	rel. energy (kcal/mol)	ρ_{Fe}	ρ_{oxo}	Fe–O_{oxo}	Fe–O_{carbox}[b]	Fe–O_{carbox}[b]	Fe–N_{eq}	Fe–N_{ax}
1	2	0	3.14	0.60	1.64	1.93/3.71	2.12/2.26	2.11	2.13
2	2	0.9	3.17	0.60	1.65	1.90/4.08	2.18/2.20	2.15	2.14
3	2	2.2	3.18	0.60	1.65	1.89/4.07	2.09/2.29	2.18	2.14
4	2	1.3	3.13	0.64	1.65	1.96/3.40	2.05/2.41	2.11	2.12
5	2	1.3	3.13	0.61	1.65	1.89/3.81	1.89/3.74	2.13	2.13
6	1	26.3	1.53	0.54	1.62	1.92/4.05	1.89/3.44	2.04	2.11
7	1	17.9	1.47	0.59	1.61	1.94/4.05	1.95/3.42	1.93	2.12
8	1	18.6	1.31	0.76	1.62	1.92/3.43	1.96/3.63	1.91	2.14
9	1	7.0	1.24	0.84	1.65	1.92/4.06	2.04/2.06	1.96	2.16

[a] All bond distances are given in Å. [b] Distances to the two oxygen atoms of the carboxylate ligands.

Table 2. Spectroscopic Parameters Calculated for **1**−**9** and Experimentally Determined Parameters for **J** from Wild-Type TauD

	S	δ (mm/s)	ΔE_Q (mm/s)	η	$A_1/g_N\beta_N$ (T)	$A_2/g_N\beta_N$ (T)	$A_3/g_N\beta_N$ (T)	D (cm^{-1})	E/D
1	2	+0.27	−0.65	0.40	−22.2	−21.4	−34.4	+3.34	0.02
2	2	+0.26	−0.72	0.10	−20.6	−18.7	−31.9	+3.57	0.10
3	2	+0.24	−0.71	0.25	−18.4	−15.3	−28.7	+3.34	0.14
4	2	+0.27	−0.82	0.52	−21.5	−19.6	−33.5	+3.74	0.09
5	2	+0.17	−0.77	0.59	−22.5	−14.8	−9.5	+2.39	0.25
6	1	+0.13	−2.15	0.93	−13.6	−11.3	+4.8	+5.22	0.11
7	1	+0.07	+1.90	0.92	−16.9	−14.8	+2.9	+5.84	0.05
8	1	+0.13	−1.39	0.83	−18.0	−19.6	+0.5	+10.85	0.03
9	1	+0.15	+0.61	0.44	−22.0	−24.4	−3.5	+7.75	0.01
expmt[39]	2	+0.31	−0.88	0	−18.0	−18.0	−18.0	+10.5	<0.03
reeval	2	+0.30[97]	−0.90[97]	0	−18.4	−17.6	−31.0	+10.5	0.01

anti) and (*anti*, *anti*) binding mode. **4** has a trigonal bipyramidal Fe-center with an axial oxo ligand and is almost identical to the model that we reported previously.[39] **5** is similar to **7** and also best described as a five-coordinate, square-pyramidal complex with an equatorial oxo ligand. For the remaining high-spin structures, **1**−**3**, one carboxylate coordinates the Fe as a monodentate ligand in the *anti* coordination mode, whereas the second carboxylate serves as a chelating, bidentate ligand, resulting generally in a distorted-octahedral geometry. For **1**, the chelating carboxylate coordinates asymmetrically ($\Delta = 0.14$ Å), with the short Fe−O bond bisecting the angle defined by the other two Fe ligand bonds of the equatorial plane. The long Fe−O bond is *trans* to the monodentate carboxylate. These geometries are best described as distorted trigonal bipyramidal. In structure **2**, the chelating carboxylate coordinates the Fe center nearly symmetrically ($\Delta = 0.02$ Å), resulting in a distorted octahedral coordination geometry that is similar to that of **9** except for the longer Fe−O bonds of the chelating carboxylate. Finally, in **3** the bidentate carboxylate coordinates the Fe center asymmetrically ($\Delta = 0.20$ Å), but in contrast to structure **1**, the shorter Fe−O bond is *trans* to the monodentate carboxylate, and the longer Fe−O bond is approximately *trans* to the equatorial imidazole. All nine structures are nearly isoenergetic and have similar Fe−O_{oxo} bond lengths, which are all in agreement with the experimentally determined Fe−O_{oxo} bond length of 1.62 Å.[29] The calculated energies of the structures lie within 2−6 kcal/mol of one another, which is within the range of error typically quoted for the B3LYP method applied to transition metal complexes.[78] Additional, larger uncertainties that arise with respect to spin-state energetics determined by DFT

(78) Siegbahn, P. E. M. *J. Biol. Inorg. Chem.* **2006**, *11*, 695−701.

methods are discussed in, for example, ref 64 and references therein. Finally, the neglect of the protein environment introduces another source of error in the calculated total energies. What the calculations confirm is that total energy cannot, by itself, be used as a basis to distinguish the correct structure from among a family of closely related candidates. However, as has been emphasized recently,[64] the calculation of spectroscopic parameters that are sensitive to differences in electronic structure caused by relatively subtle differences in geometric structure may be used to provide more stringent geometrical constraints. As shown below, the comparison of the spectroscopic parameters predicted by computation for each structure to those experimentally determined by Mössbauer spectroscopy does indeed provide insight into the structure of **J**.

Comparison of the Calculated and Experimental Spectroscopic Parameters of Intermediate J from Wild-Type TauD. To choose the best model for **J** from among the isoenergetic structures **1**−**9**, spectroscopic parameters were calculated for each model and compared to the measured values. The isomer shift and quadrupole splitting of **J** have experimental uncertainties of ∼0.02 mm/s and ∼0.03 mm/s.[39] Computational uncertainties of ∼0.1 mm/s (δ)[41] and ∼0.5 mm/s (ΔE_Q)[79] have been estimated from studies of a large number of structurally defined Fe complexes spanning a wide variety of coordination geometries and oxidation states. Experimentally, η does not affect the simulated spectra of **J** significantly, because ΔE_Q and thus all three components of the EFG are small. Consequently, it could not be determined and was, as in our previous analysis, assumed to be zero due to the strongly donating axial oxo ligand. The *x*- and *y*-component of the $\mathbf{A}/g_N\beta_N$-tensor were determined with good precision experimentally (the uncertainty is approximately 0.3 T and is caused by the uncertainty in E/D, which in turn results in uncertainty of the spin expectation values $\langle S_x\rangle$ and $\langle S_y\rangle$), due to the large spin expectation value of the axial $S = 2$ ground state in the *x*- and *y*-directions, but the *z*-component was not determined, due to the small magnitude of the spin expectation value, $\langle S_z\rangle$.[39] Computationally, the anisotropic contribution to the **A**-tensor can be determined with accuracy, whereas the isotropic Fermi contact term is typically significantly underestimated.[43] However, a correction factor of 1.69 for the Fermi contact contribution was previously shown to provide results that are in good agreement with a large body of experimental data.[43] The zero-field splitting parameters D and E/D have been determined accurately from the field-dependent spectra for **J**.[39] The calculated D-values are significantly less than the experimental value of 10.5 cm^{-1}. This underestimation of D was also found in previous work on heme Fe(IV)-oxo species with an $S = 1$ ground state.[40,44,73,80] More accurate values for D can be obtained from correlated *ab initio* calculations.[73,81]

Structures **6**−**9** with a triplet ground state are ruled out as candidates for the structure of **J** because their predicted spectroscopic parameters are clearly incompatible with the experimental data. As we reported previously, the large internal magnetic fields observed experimentally for **J** can be simulated with an $S = 1$ spin Hamiltonian with unusually large, negative hyperfine couplings ($A_x/g_N\beta_N \approx A_y/g_N\beta_N \approx -33$ T).[26] However, the calculated values of $A_x/g_N\beta_N$ and $A_y/g_N\beta_N$ for **6**−**9** (average ∼ −19 T) are close to the Fermi contact term, and the absolute magnitude is too small to explain the experimentally observed internal magnetic field. Thus, the calculation provides strong evidence against the triplet structures. In addition, the calculated isomer shifts are significantly (on average, 0.19 mm/s) less than the experimental value and outside of the typical range of uncertainty (0.1 mm/s). Finally, except for that of **8**, the quadrupole splitting parameters do not agree with the experimental value.

For the quintet structures, the five-coordinate complex **5** is ruled out as a model for **J**, because (1) the isomer shift is 0.13 mm/s less than the experimental value, (2) the anisotropy of the *x*- and *y*-component of the **A**-tensor is much greater than the experimentally observed value, and (3) the calculated rhombicity is much greater than the experimental value. For the remaining quintet structures, **1**−**4**, the predicted Mössbauer isomer shifts and quadrupole splittings are in agreement with the experimental values.[82] For all four structures nearly axial **A**-tensors are calculated, of which the *x*- and *y*-components are close to the Fermi contact term: $A_x/g_N\beta_N \approx A_y/g_N\beta_N \approx -20$ T. The *z*-component is predicted to be approximately 12 T more negative than the *x*- and *y*-components: $A_z/g_N\beta_N \approx -32$ T. The D-values calculated by the BP86 functional in combination with the Pederson and Khanna method[72] are consistently less than the experimentally observed value ($D = 10.5$ cm^{-1}). We therefore undertook the significant computational effort to apply the SORCI method, a simplified multireference configuration interaction variant described in ref 83. We applied the thresholds $T_{pre} = 1 \times 10^{-4}$, $T_{sel} = 1 \times 10^{-6}$, $T_{nat} = 1 \times 10^{-5}$ together with the SOC treatment of ref 81 to our favorite structures **1** and **2**. The obtained D-values (8.6 cm^{-1} and 8.7 cm^{-1} for **1** and **2**, respectively) are indeed in good agreement with the experimental value. The major contribution to D arises from the interaction with the low-lying triplet state, as discussed in detail previously.[40,44] The remaining computed parameters, η and E/D, vary significantly for **1**−**4**. Experimentally, the Mössbauer spectra are not sensitive to variations of η, because ΔE_Q is small, and consequently, the principal components of the electric field gradient are small. The other parameter, E/D, was determined experimentally to be less than 0.03. Taking the predicted E/D values at face value, only **1** is compatible with the field-dependent Mössbauer spectra, but given the uncertainty in predicting this parameter computationally, we cannot rule out structures **2**−**4** as reasonable models for **J**.

For structures **1**−**4**, the calculations predict that the *z*-component of the $\mathbf{A}/g_N\beta_N$-tensor should be 12−13 T more negative than the *x*- and *y*-components. As was noted previously, $A_z/g_N\beta_N$ cannot be determined from the field-dependent 4.2-K Mössbauer spectra, because the lowest-energy state of the nearly axial integer-spin system with $D > 0$ exhibits only a small $\langle S_z\rangle$.[35,39] The excited states of the $S = 2$ manifold, however, exhibit large $|\langle S_z\rangle|$ values, which, in the slow relaxation limit, will result in magnetically split spectra that would allow for determination of $A_z/g_N\beta_N$. Spurred by the prediction that $A_z/g_N\beta_N$ for model structures **1**−**4** is considerably larger in

(79) Godbout, N.; Havlin, R.; Salzmann, R.; Debrunner, P. G.; Oldfield, E. *J. Phys. Chem. A* **1998**, *102*, 2342−2350.
(80) Reviakine, R.; Arbuznikov, A. V.; Tremblay, J.-C.; Remenyi, C.; Malkina, O. L.; Malkin, V. G.; Kaupp, M. *J. Chem. Phys.* **2006**, *125*, 054110.
(81) Ganyushin, D.; Neese, F. *J. Chem. Phys.* **2006**, *125*, 024103.
(82) Structure **4** is similar to the trigonal bipyramidal model reported previously.[39] The larger isomer shift of **4** ($\delta = 0.27$ δmm/s) compared to that reported before ($\delta = 0.22$ mm/s) is caused by slightly longer (on average 0.07 Å) $Fe-O_{carboxylate}$ distances, as noted before.[41]
(83) Neese, F. *J. Chem. Phys.* **2003**, *119*, 9428−9443.

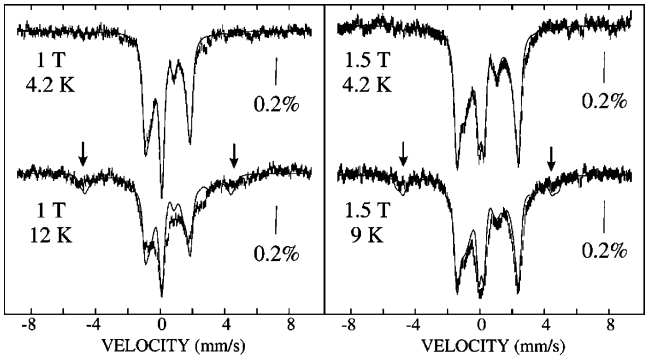

Figure 2. Mössbauer spectra of intermediate **J**, recorded at 1 T (left) and 1.5 T (right) at 4.2 K (top) and an elevated temperature (12 K/1 T and 9 K/1.5 T). The contribution of the reactant complex (20% of the total intensity) acquired under the same conditions has been removed from the experimental spectra (not shown). Solid lines are simulations according to the spin Hamiltonian formalism in the slow-relaxation limit and parameters in Table 2.

magnitude than that for structures **5**−**9**, potentially providing an additional basis for discriminating among the models, we attempted to resolve this parameter by acquiring Mössbauer spectra of a sample containing 80% of intermediate **J** and 20% of the reactant complex at various temperatures and magnetic fields. Spectra in external fields of 1 T (left) and 1.5 T (right) at 4.2 K (top) and a temperature sufficiently high to populate excited states with greater $\langle S_z \rangle$ (bottom) are shown in Figure 2. These were obtained after removal of the contribution of the spectrum of the reactant complex under the same conditions. As indicated by the arrows, new features from **J** appear at higher temperature. The splitting of the excited state is proportional to $A_z/g_N\beta_N \cdot \langle S_z \rangle$, and because only $\langle S_z \rangle$ depends on the magnitude of the externally applied magnetic field, it is, in principle, possible to determine both quantities, $A_z/g_N\beta_N$ and $\langle S_z \rangle$, from spectra recorded at two magnetic fields. $\langle S_z \rangle$, in turn, depends strongly on the rhombicity, E/D (Figure S1). However, spectra at elevated temperatures (Figures 2 and S2) suggest that relaxation of the electronic states is not strictly in the slow-relaxation regime. For the spectra shown, this is evident from the broadening of the features associated with the electronic ground state at the elevated temperature (compare top and bottom spectra). Although the intermediate relaxation regime precludes an accurate determination of E/D and $A_z/g_N\beta_N$, the magnitude of the splitting clearly corroborates the prediction of the DFT calculations that $A_z/g_N\beta_N$ is large and negative, thus supporting the notion that models **1**−**4** more closely mimic the structure of **J** than do **5**−**9**. Spectral simulations based on the parameters given in Table 2 and the assumption of slow relaxation (solid lines in Figure 2) can account reasonably well for both the new field- and temperature-dependent spectra and the field-dependent spectra reported previously.

The best agreement between theory and experiment was found for the six-coordinate, high-spin structure **1**. The calculated Fe−O_{oxo} distance of 1.65 Å is close to the experimental value of 1.62 Å obtained by extended X-ray absorption fine structure (EXAFS) spectroscopy, and is similar to the Fe−O_{oxo} bond distances observed in Fe(IV)-containing heme enzyme intermediates, inorganic heme complexes,[84−88] and nonheme models.[32−34,89,90] Although all of those species have an $S = 1$ ground state, it was recently recognized that the Fe−O_{oxo} bond length is comparable for ferryl species with $S = 1$ and $S = 2$

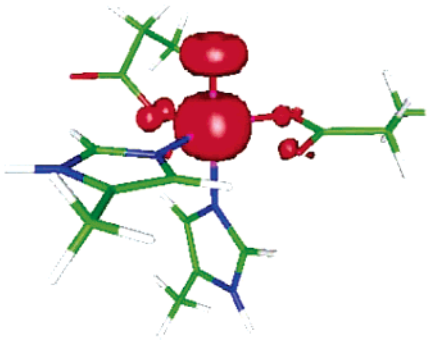

Figure 3. Spin density of **1**. Positive spin densities are displayed in red, and negative spin densities, in yellow. The greatest spin density was found at the iron centers, followed by the O_{oxo} atom, and by the other O-atoms in decreasing order. A cutoff of 0.01 au was employed for the spin density plot.

ground states.[40,91] Within a few degrees, the short Fe−O_{oxo} bond defines the *z*-axis of the electric field gradient, zero-field splitting, and ^{57}Fe hyperfine tensors. As expected, the spin populations at the Fe and O_{oxo} atoms are large, +3.14 and −0.60, respectively (Figure 3). They compare nicely with the results on the hypothetical high-spin Fe(IV)-oxo species obtained by Ghosh, et al.[92] The molecular orbital (MO) diagram for the complex (Figure 4) closely resembles results obtained elsewhere (refs 40, 44, 91, and 93 and references cited therein). In order of decreasing orbital energy, the MO diagram displays an empty antibonding σ^* orbital that consists primarily of the iron d_{z^2} atomic orbital (AO) and an oxo p_z-AO. The next lowest MOs are singly occupied and are formed by the $d_{x^2-y^2}$ orbital, by antibonding π^*-combinations of the d_{xz} or d_{yz} and oxo $p_{x,y}$-AOs, and by the d_{xy} metal AO. Selected doubly occupied ligand orbitals are also displayed in Figure 4.

Oxygen Activation by His99Ala-TauD. Substitution of iron ligands potentially affords a tool to perturb both the structure and the spectroscopic parameters of an iron site and thereby to provide additional constraints for deducing its structure. Substitution by alanine or glycine has been used to open a site into which small-molecule ligands can insert, thereby enabling more subtle variation of the nature of the ligand. Substitution of His99, a ligand anticipated to be *cis* to the oxo group in **J**, by alanine was attempted with this rationale. Surprisingly, His99Ala-TauD is catalytically active, even in the absence of imidazole. The turnover number of 0.5 s^{-1} (at 5 °C with other conditions as previously described[26]) is less than the value of 1.3 s^{-1} for the

(84) Penner-Hahn, J. E.; McMurry, T. J.; Renner, M.; Latos-Grazynsky, L.; Eble, K. S.; Davis, I. M.; Balch, A. L.; Groves, J. T.; Dawson, J. H.; Hodgson, K. O. *J. Biol. Chem.* **1983**, *258*, 12761−12764.
(85) Chance, B.; Powers, L.; Ching, Y.; Poulos, T.; Schonbaum, G. R.; Yamazaki, I.; Paul, K. G. *Arch. Biochem. Biophys.* **1984**, *235*, 596−611.
(86) Penner-Hahn, J. E.; Smith Eble, K.; McMurry, T. J.; Renner, M.; Balch, A. L.; Groves, J. T.; Dawson, J. H.; Hodgson, K. O. *J. Am. Chem. Soc.* **1986**, *108*, 7819−7825.
(87) Wolter, T.; Meyer-Klaucke, W.; Müther, M.; Mandon, D.; Winkler, H.; Trautwein, A. X.; Weiss, R. *J. Inorg. Biochem.* **2000**, *78*, 117−122.
(88) Stone, K. L.; Behan, R. K.; Green, M. T. *Proc. Natl. Acad. Sci. U.S.A.* **2005**, *102*, 16563−16565.
(89) Nam, W.; Choi, S. K.; Lim, M. H.; Rohde, J.-U.; Kim, I.; Kim, J.; Kim, C.; Que, L., Jr. *Angew. Chem., Int. Ed.* **2003**, *42*, 109−111.
(90) Rohde, J.-U.; Torelli, S.; Shan, X.; Lim, M. H.; Klinker, E. J.; Kaizer, J.; Chen, K.; Nam, W.; Que, L., Jr. *J. Am. Chem. Soc.* **2004**, *126*, 16750−16761.
(91) Decker, A.; Clay, M. D.; Solomon, E. I. *J. Inorg. Biochem.* **2006**, *100*, 697−706.
(92) Ghosh, A.; Tangen, E.; Ryeng, H.; Taylor, P. R. *Eur. J. Inorg. Chem.* **2004**, 4555−4560.
(93) Conradie, J.; Tangen, E.; Ghosh, A. *J. Inorg. Biochem.* **2006**, *100*, 707−715.

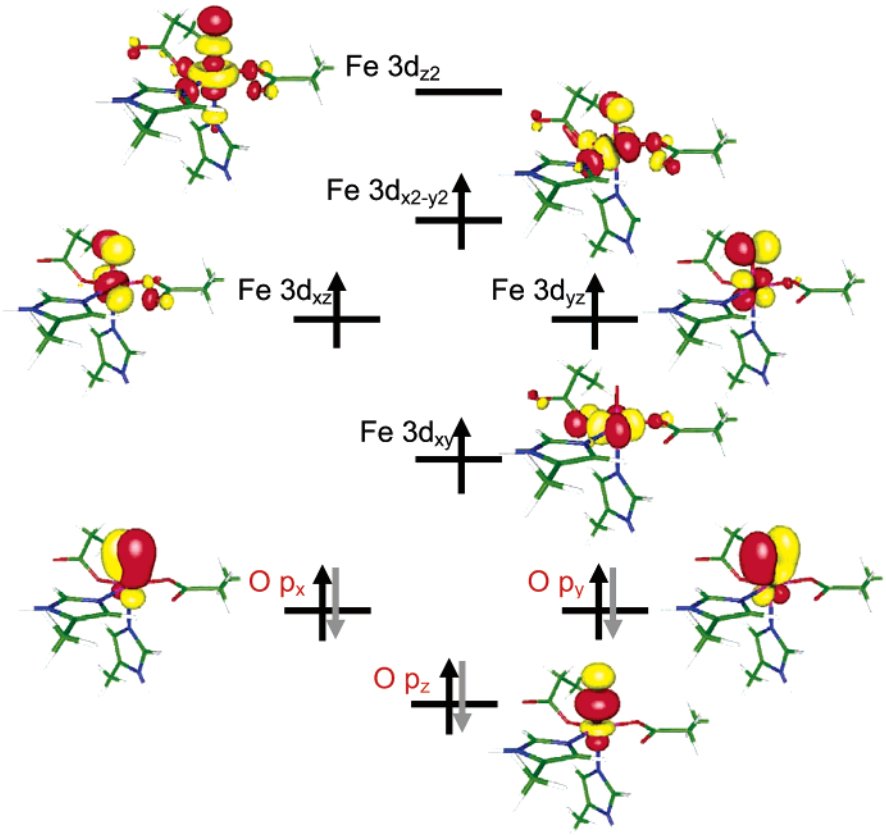

Figure 4. Schematic MO diagram of **1**. Quasi restricted orbitals were employed. Cutoffs of 0.05 au were used.

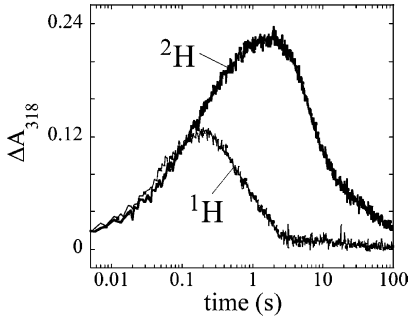

Figure 5. Reaction of the His99Ala-TauD•Fe(II)•αKG•taurine complex with O_2 monitored by absorbance at 318 nm. A solution of the quaternary complex (prepared with either unlabeled taurine (thin line) or 1,1-[^{2}H]$_2$-taurine (bold line)) was reacted with an equal volume of an O_2-saturated buffer solution at 5 °C. Concentrations after mixing were as follows: [His99Ala-TauD] = 0.5 mM; [Fe] = 0.4 mM, [αKG] = 5 mM, [taurine] = 1 mM; [O_2] = 0.6 mM.

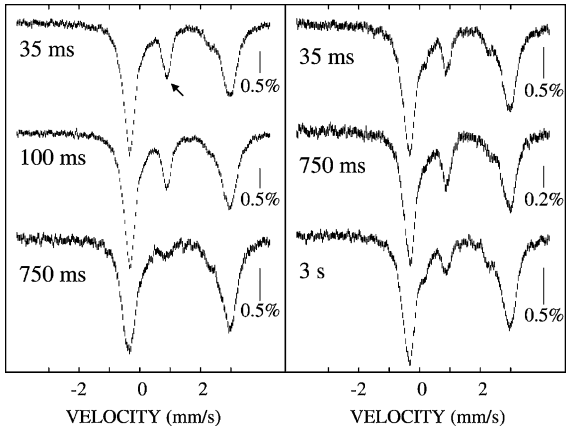

Figure 6. 4.2-K/53-mT Mössbauer spectra of selected samples prepared by the freeze-quench method. A solution of the quaternary His99Ala-TauD•Fe(II)•αKG•taurine complex (prepared with either unlabeled taurine (left panel) or 1,1-[^{2}H]$_2$-taurine (right panel)) was reacted with an equal volume of an O_2-saturated buffer solution at 5 °C. Concentrations after mixing were as follows: [His99Ala-TauD] = 2.0 mM; [Fe] = 1.7 mM, [αKG] = 7.5 mM, [taurine] = 7.5 mM; [O_2] = 1.0 mM. Reaction times are indicated at the respective spectrum.

wild-type enzyme. Addition of the cosubstrate, αKG, to a solution containing equimolar His99Ala-TauD and Fe(II) elicits the characteristic metal-to-ligand charge transfer (MLCT) band at 530 nm, indicating that αKG binds to the Fe(II) center of the His99Ala-TauD•Fe(II) complex in the usual chelating mode (Figure S3).[94] Titrations allowed a dissociation constant (K_D) for αKG of 30 μM to be estimated. Upon rapid mixing at 5 °C of the His99Ala-TauD•Fe(II)•αKG•taurine complex with O_2-saturated buffer, an absorption feature centered at 318 nm, which in the reaction of the wild-type protein is known to be associated with **J**, develops and decays (Figure 5, thin line). Use of 1,1-[^{2}H]$_2$-taurine as a substrate under identical reaction conditions results in a much greater amplitude and much slower decay of this transient feature (Figure 5, bold line), indicative of a large substrate deuterium kinetic isotope effect on decay of the associated complex. This interpretation was verified by freeze-quench Mössbauer experiments with both unlabeled (Figure 6, left panel) and deuterated taurine (Figure 6, right panel). A transient absorption line at 0.9 mm/s (indicated by arrow) is observed in the 4.2-K/53-mT Mössbauer spectra. This new peak persists longer in the reaction with deuterated substrate (compare spectra of 750-ms samples), establishing that the associated

(94) Pavel, E. G.; Zhou, J.; Busby, R. W.; Gunsior, M.; Townsend, C. A.; Solomon, E. I. *J. Am. Chem. Soc.* **1998**, *120*, 743−753.

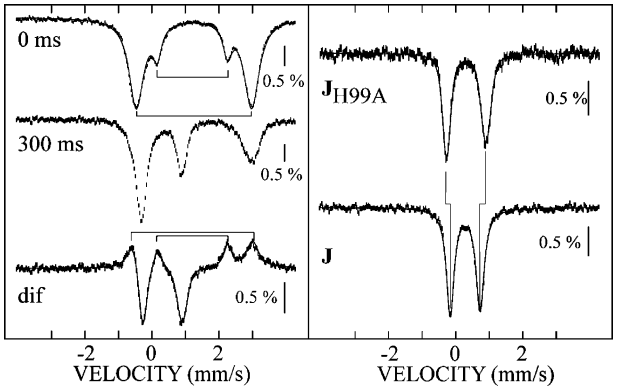

Figure 7. 4.2-K/53-mT Mössbauer spectra of the quaternary His99Ala-TauD•Fe(II)•αKG•1,1-[^{2}H]$_2$-taurine complex (top) and a sample that was freeze-quenched 300 ms after mixing this complex at 5 °C with a double volume of an O_2-saturated buffer solution. Concentrations after mixing were as follows: [His99Ala-TauD] = 1.6 mM; [Fe] = 1.3 mM, [αKG] = 5 mM, [taurine] = 5 mM; [O_2] = 1.3 mM.

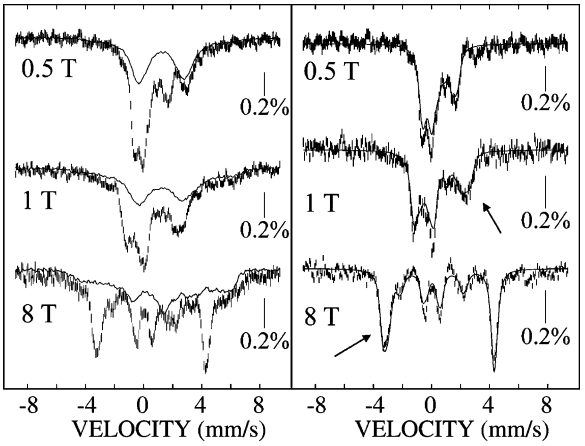

Figure 8. 4.2-K/variable-field Mössbauer spectra of the Fe(IV) intermediate in His99Ala-TauD. Left panel: Spectra of the 300-ms sample described in Figure 7 (hashed marks) and the reactant complex (solid lines, scaled to 50% of the intensity). Right panel: spectra of the Fe(IV) intermediate in His99Ala-TauD (hashed marks) and simulations according to the spin Hamiltonian formalism and parameters given in Table 4 (solid lines).

complex abstracts hydrogen. The analogy of these observations to those on **J** in the reaction of the wild-type protein implies that the transient species in His99Ala-TauD is also a ferryl complex. Its Mössbauer spectroscopic properties (see below) are consistent with this assignment.

Characterization of the Fe(IV) Intermediate in His99Ala-TauD by Mössbauer Spectroscopy. The 4.2-K/53-mT Mössbauer spectrum of the reactant His99Ala-TauD•Fe(II)•αKG•taurine complex (Figure 7, top left) consists of two broad quadrupole doublets with parameters typical of high-spin Fe(II) sites: $\delta(1) = 1.26$ mm/s, $\Delta E_Q(1) = 3.44$ mm/s, 85 ± 3% of total intensity and $\delta(2) = 1.21$ mm/s, $\Delta E_Q(2) = 2.10$ mm/s, 15 ± 3% of total intensity. The presence of (at least) two quadrupole doublets indicates that at least two distinct complexes are present and contrasts with the situation for wild-type TauD, for which only one quadrupole doublet is observed. Subtraction of the spectrum of the reactant complex from the spectrum of a sample freeze-quenched 300 ms after this complex was mixed with O_2-saturated buffer reveals that the intermediate exhibits a quadrupole doublet (Figure 7, bottom spectrum in left panel). The isomer shift, $\delta = 0.31$ mm/s, is not significantly different from that of **J**, whereas the quadrupole splitting parameter, $\Delta E_Q = 1.17$ mm/s, is significantly greater. The similarity of the Mössbauer features (see Figure 7, right panel) suggests that the intermediate in His99Ala-TauD is a ferryl complex similar to **J** but perturbed by the absence of the His99 ligand. This species forms at the expense of two distinct Fe(II) species with parameters $\delta(1) = 1.26$ mm/s, $\Delta E_Q(1) = 3.56$ mm/s and $\delta(2) = 1.20$ mm/s, $\Delta E_Q(2) = 2.08$ mm/s. The lost intensity from these Fe(II) species corresponds to 31 ± 3% and 17 ± 3%, respectively, of the total intensity of the spectrum of the reactant complex. Notably, the Fe(II) complex denoted 2 (with smaller ΔE_Q) disappears entirely within the 300-ms reaction time, whereas species 1 does not, suggesting either that 2 is somewhat more reactive than 1 or that 2 is exclusively reactive and 1 converts to 2 prior to reaction with O_2.

Mössbauer spectra of the His99Ala-TauD Fe(IV) complex in externally applied fields of 0.5, 1, and 8 T (Figure 8, right panel) were generated from the field-dependent spectra of the 300-ms sample (Figure 8, left panel) by subtracting the 50% contribution of the remaining reactant complex (solid lines in left panel). The heterogeneity in the reactant and different reactivity of its component complexes introduce greater-than-usual uncertainty in the subtraction analysis. However, because the spectra of the Fe(II)-containing reactant species in externally applied magnetic fields are broad, whereas the Fe(IV) intermediate exhibits much sharper features, the analysis suffices to reveal the magnitude of the magnetic hyperfine splitting in the spectrum. The magnitude of the splitting observed for the 8-T spectrum is comparable to that for **J**, indicating that the Fe(IV) intermediate in His99Ala-TauD also has a high-spin ($S = 2$) ground state. The 0.5 and 1 T spectra exhibit greater splitting than do the corresponding spectra of **J**, a behavior that can be rationalized by comparing the D-values of the two complexes. For the variant, the smaller D-value results in larger $|\langle S_{xy}\rangle|$ values in external fields of 0.5 and 1 T, but the difference in $\langle S_{xy}\rangle$ is diminished by increasing magnetic field. The peaks (in particular, those indicated by arrows) are also broader than those of **J**. This is indicative of greater anisotropy within the xy-plane for the Fe(IV) intermediate in the variant. This behavior is reflected in the simulation parameters, in particular the significantly greater rhombicity (E/D) of 0.07. The solid lines in the right panel are simulations according to the spin Hamiltonian formalism in the slow relaxation limit and the parameters given in Table 4. The z-component of the **A**-tensor was fixed at −30 T, a value 13 T more negative than the average of the x- and y-component, on the basis of the computational results (see below).

Computational Studies of the Fe(IV) Intermediate in His99Ala-TauD. DFT calculations were carried out to rationalize the perturbations to the electronic structure and spectroscopic parameters of the Fe(IV) intermediate caused by the ligand substitution. For the model structures, the deleted imidazole ligand was replaced with either water or hydroxide, the most likely candidates to coordinate to the Fe center in lieu of His99. Structures with a quintet ground state and either a water ligand (**10**−**13**) or a hydroxide ligand (**14** and **15**) were calculated. In addition, structures with a triplet ground state and a water ligand were calculated (**16** and **17**). The structures are shown in Figure 9. Mulliken spin populations and important geometrical parameters for **10**−**17** are compared in Table 3, and calculated and

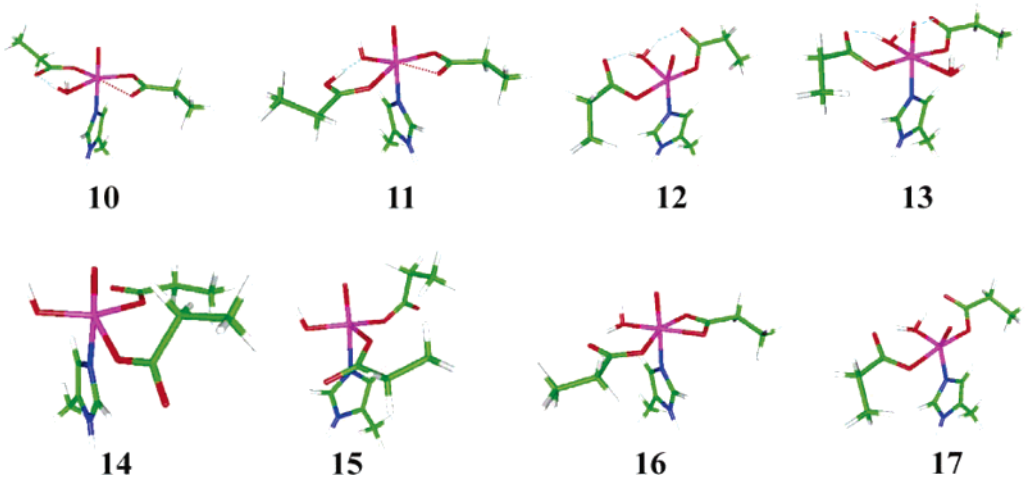

Figure 9. Geometry optimized models of the Fe(IV) intermediate in His99Ala-TauD. Structures **10** through **15** are quintet states, and structures **16** and **17** are triplet states. Color code: iron (magenta), oxygen (red), nitrogen (blue), carbon (green), hydrogen (gray). The red dotted lines in **10** and **11** represent the longer Fe−O bond of the chelating carboxylate ligand. The cyan dotted lines represent hydrogen bonds.

Table 3. Mulliken Spin Populations ρ and Geometrical Parameter of Structures **10**−**17** from Figure 9 as a Model for the Fe(IV) Intermediate from His99Ala-TauD[a]

	S	rel. energy (kcal/mol)	ρ_{Fe}	ρ_{oxo}	Fe–O_{oxo}	Fe–O_{carbox}[b]	Fe–O_{carbox}[b]	Fe–N_{ax}	Fe–O_{wat}
10	2	0	3.17	0.62	1.64	2.08/2.22	2.03/3.27	2.10	2.08
11	2	0.7	3.16	0.64	1.64	2.10/2.20	2.17/3.29	2.10	1.95
12	2	2.7	3.13	0.69	1.65	1.94/3.19	1.93/3.19	2.10	2.09
13	2	47 950	3.19	0.62	1.65	1.95/3.19	2.04/3.26	2.09	2.09/2.31
14	2	338.7	3.21	0.52	1.65	2.00/4.00	2.04/3.28	2.14	1.86
15	2	339.4	3.22	0.51	1.66	2.06/3.42	1.97/4.18	2.13	1.87
16	1	5.8	1.23	0.84	1.65	2.00/2.03	1.96/3.20	2.11	1.99
17	1	11.4	1.53	0.50	1.61	1.98/3.15	1.97 /3.15	2.07	1.88

[a] All bond distances are given in Å. [b] Distances to the two oxygen atoms of the carboxylate ligands.

Table 4. Spectroscopic Parameters Calculated for **10**−**17** and Experimentally Determined Parameters for **J** from His99Ala-TauD

	S	δ (mm/s)	ΔE_Q (mm/s)	η	$A_x/g_N\beta_N$ (T)	$A_y/g_N\beta_N$ (T)	$A_z/g_N\beta_N$ (T)	D (cm^{-1})	*E*/*D*
10	2	+0.29	−1.24	0.52	−19.9	−21.9	−34.0	+3.54	0.08
11	2	+0.24	−1.27	0.50	−14.8	−18.5	−29.1	+3.79	0.12
12	2	+0.17	−1.36	0.42	−6.9	−13.9	−21.0	+2.99	0.29
13	2	+0.25	−1.21	0.26	−15.9	−20.1	−30.3	+3.90	0.16
14	2	+0.15	−0.31	0.77	−14.4	−17.2	−26.8	+2.71	0.19
15	2	+0.16	−0.32	0.84	−13.7	−16.8	−26.0	+2.54	0.24
16	1	+0.19	+0.29	0.43	−21.7	−23.5	−3.1	+8.80	0.01
17	1	+0.08	+2.14	0.24	−7.6	−12.6	+6.6	+3.22	0.10
expmt	2	+0.31	−1.17	0.75	−18.1	−16.1	−31	+8.0	0.07

experimentally determined spectroscopic parameters are compared in Table 4.

All structures have in common that the imidazole ligand representing His255 is *trans* to the oxo group. In **10**, the ligands in the equatorial plane are an asymmetrically coordinated, bidentate carboxylate ligand (Δ = 0.14 Å), a monodentate carboxylate in the *syn* mode, and the water ligand. One of the H-atoms of the coordinated water is engaged in a hydrogen bond with the uncoordinated oxygen of the monodentate carboxylate ligand. The geometry of **10** is best described as distorted octahedral. The coordination environment of **11** is similar to that of **10**, but **11** is effectively a tautomer of **10** in which the proton of the H-bond between the coordinated water and the monodentate carboxylic acid is closer to the carboxylic acid. Consequently, the Fe−OH bond shortens by 0.05 Å. In structure **12**, both carboxylate ligands coordinate the Fe-center in a *syn*-monodentate fashion, and the uncoordinated O-atoms of the carboxylate groups are involved in hydrogen bonds with the coordinated water. The resulting structure is best described as five-coordinate, square pyramidal, with the water ligand in the apical position and the oxo ligand in the equatorial plane. In structure **13**, a second water ligand was added to structure **12**, resulting in a distorted octahedral complex. The structures with a hydroxide ligand serving as the exogenous "rescue" ligand, **14** and **15**, are best described as trigonal bipyramidal complexes with apical oxo and imidazole ligands and the hydroxide and two carboxylate ligands (one coordinating in the *syn* mode and the other in the *anti* mode) in the equatorial plane. Interestingly, the proton of the hydroxide ligand fails to form a H-bond with a carboxylate, resulting in a dihedral angle H−$O_{hydroxo}$−Fe−O_{oxo} of approximately 0°. One of the key structural features of both **14** and **15** is the shorter Fe−$O_{hydroxo}$ bond.

Triplet structures **16** and **17** are similar to **10** and **12**, respectively. As was observed for the model structures of the wild-type intermediate **J**, structures **10**−**17** have similar total energies, thus precluding use of total energy alone as a criterion for choosing the most likely structure for the Fe(IV) intermediate in His99Ala-TauD.

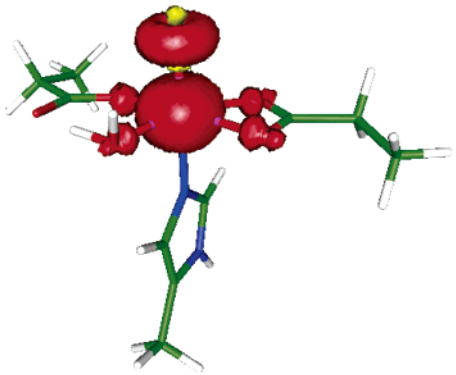

Figure 10. Spin densities in **10**. Positive spin densities are displayed in red, and negative spin densities, in yellow. The greatest spin density was found at the iron center, followed by the O_{oxo} atom, and by the other O-atoms in decreasing order. A cutoff of 0.01 au was employed for the spin density plot.

Comparison of the Calculated and Experimental Spectroscopic Parameters of the Fe(IV) Intermediate in His99Ala-TauD. As for the model structures for **J**, triplet structures **16** and **17** can be ruled out on the basis of (1) their low isomer shifts (0.12 and 0.21 mm/s less than the experimental value, respectively); (2) their quadrupole splittings, which deviate by more than 1.3 mm/s from the experimental value; and (3) the excessively large values (~ -33 T) for the *x*- and *y*- components of their $\mathbf{A}/g_N\beta_N$-tensor that would be required to account for the large magnetic splitting in the 8-T spectrum. The quintet structures that have a hydroxide ligand replacing His99, **14** and **15**, can also be ruled out as candidate structures, on the basis of (1) their low isomer shifts, which are a direct consequence of their shorter $Fe-O_{hydroxide}$ bonds, and (2) their quadrupole splittings, which are approximately 0.8 mm/s more positive than the experimental value. The remaining structures have a quintet ground state and a water ligand replacing the imidazole of His99. Of these structures, only **12** can be excluded as a candidate, on the basis of its low isomer shift and excessively anisotropic **A**-tensor (which is a consequence of its unusual square-pyramidal structure with the equatorial oxo ligand). For the remaining three models, **10**, **11**, and **13**, the isomer shifts are sufficiently large ($\delta > 0.20$ mm/s), the quadrupole splittings are all ~ -1.2 mm/s, the **A**-tensors are axial with large negative z-components, the *D* values are positive, and the rhombicities *E*/*D* are moderate, ranging from 0.08 to 0.16. The parameters predicted for **10** are in best agreement with the experimental values, and we consider **10** to be the best model for the Fe(IV) intermediate in His99Ala-TauD. We disfavor **13** as a model, because the agreement between theory and experiment is not as good as that for our preferred structure, **10**. Moreover, **13** contains *two* water ligands, which we consider less likely because this would require either that both water ligands be present in the starting complex or that the second water molecule coordinate the Fe-center during the conversion of the reactant complex to the Fe(IV)-oxo intermediate. Of the two tautomers **10** and **11**, **10** has the greater isomer shift as a consequence of the longer $Fe-O_{water}$ bond, the smaller difference between the *x*- and *y*-components of its **A**-tensor, and the lesser rhombicity. All three parameters thus favor **10** relative to **11** as a model for the Fe(IV) intermediate in His99Ala-TauD. The spin populations on the Fe and O_{oxo} atoms of **10** are large, +3.17 and −0.62, respectively (Figure 10), and agree with the corresponding values obtained for **1**, our preferred model for the wild-type intermediate, **J**.

Comparison of the Structures of the Fe(IV)-oxo Intermediates. The structures that match the experimental data of the Fe(IV) intermediates in wild-type and His99Ala-TauD best are the distorted octahedral complexes **1** and **10**, respectively. Other distorted octahedral (**2**, **3**, **11**, **13**) and trigonal bipyramidal (**4**) structures are consistent with the experimental data, but the agreement is not as good. Square pyramidal complexes with an equatorial oxo group (**5**, **12**) are not compatible with the experimental data. The spectroscopic parameters of **1** and **10** have been recognized as typical for high-spin Fe(IV)-oxo complexes:[40] (1) a rather high isomer shift of approximately 0.3 mm/s, which is a consequence of a weak ligand field in the *xy*-plane, (2) a negative quadrupole splitting of approximately −1 mm/s, (3) a nearly axial **A**-tensor with *x*- and *y*-components close to the Fermi contact term (~ -20 T) and a more negative *z*-component (~ -32 T), (4) a positive zero-field splitting parameter, *D*, and (5) a fairly small rhombicity, *E*/*D*. In addition, the calculations reproduce the more negative quadrupole splitting for the His99Ala-TauD complex and also reproduce the correct trend for the rhombicity. However, we note that prediction of zero-field splitting parameters (*D* and *E*/*D*) is currently still associated with relatively large uncertainties. More detailed studies of structurally well-defined model systems with known *D* and *E*/*D* values will be required to calibrate computation of these parameters. The good agreement of the experimental data with structures **1** and **10** supports the view that a water molecule replaces the equatorial histidine ligand in His99Ala-TauD. Although we have considered only the first coordination sphere of the iron in the calculations, there are subtle changes upon the replacement of imidazole with water. For example, the binding mode of the monodentate carboxylate changes, because the noncoordinating O-atom is involved in a hydrogen bond with the coordinated water. Other factors, such as subtle differences in the geometry of the active site or the presence of CO_2, the byproduct of the decarboxylation of αKG, could conceivably perturb the Fe site and result in different calculated spectroscopic parameters. These factors have not been considered thus far because of the significantly increased complexity and longer computation times.

1 and **10** have comparable spin populations on the Fe and O_{oxo} atoms. The orbitals with predominantly d_{xz} and d_{yz} character, which interact with the p_x and p_y orbitals of the O_{oxo} atom in a π-bond, are singly occupied, as in the ferryl species with an $S = 1$ ground state.[40,91] Thus, the electronic structure of the ferryl group and possibly its reactivity, which involves in many cases (including TauD) abstraction of hydrogen from an aliphatic carbon of the substrate, may be similar.[95,96]

Conclusions and Outlook

Calculation by DFT of a variety of models for the ferryl intermediates in wild-type TauD and its His99Ala ligand variant, prediction of the spectroscopic parameters of each model, and

(95) Neidig, M. L.; Decker, A.; Choroba, O. W.; Huang, F.; Kavana, M.; Moran, G. R.; Spencer, J. B.; Solomon, E. I. *Proc. Natl. Acad. Sci. U.S.A.* **2006**, *103*, 12966−12973.
(96) Decker, A.; Solomon, E. I. *Angew. Chem., Int. Ed.* **2005**, *44*, 2252−2255.
(97) More accurate determination of the isomer shift and quadrupole splitting parameter from a spectrum of a sample containing 80% of intermediate **J** yields values that are slightly different but are within the experimental uncertainty of our previously reported values.

comparison to the experimentally measured values has allowed selection of a small set of similar structures that are likely to have the important structural features of the Fe(IV) centers. The results suggest that the wild-type intermediate has a ligand sphere comprising the two His residues, the oxo group, and two carboxylates (succinate and Asp101). For the intermediate in the His99Ala variant, similar structures, in which the equatorial imidazole representing His99 is replaced with water, provide good agreement with the experimental data. The results validate the emerging approach of using a combination of spectroscopy and DFT calculations to deduce structural details of reaction intermediates.

Identification of structures for the C−H-cleaving Fe(IV)-oxo intermediate, **J**, that are consistent with the experimental data lays the foundation for more detailed computational studies of the TauD reaction cycle. Specifically, we aim to (1) understand the reaction steps between the addition of oxygen to the reactant complex and formation of **J** and (2) quantitatively evaluate the reactivity of **J** toward abstraction of hydrogen from the substrate. The TauD system is ideal for the latter endeavor, because the intrinsic deuterium kinetic isotope effect on hydrogen abstraction has been measured. These studies are ongoing.

Acknowledgment. This work was supported by the National Institutes of Health (NIH GM-69657 to J.M.B. and C.K.), the Arnold and Mabel Beckman Foundation (Young Investigator Award to C.K.), and the Dreyfus Foundation (Camille Dreyfus Teacher Scholar Award to C.K.). F.N. gratefully acknowledges funding from the priority Program 1137 of the Deutsche Forschungsgemeinschaft and the German Israeli Foundation (Project I-746-137.9/2002).

Supporting Information Available: Complete references 12 and 59; a figure displaying $\langle S_z \rangle$ of the first excited state of an $S = 2$ system with $D = 10.5$ cm^{-1} as a function of the magnetic field for various E/D values; a figure showing Mössbauer spectra of intermediate **J** from wild-type TauD recorded in an 8-T external field at $T = 4.2$ K and $T = 20$ K; a comparison of the UV−visible absorption spectra of the quaternary TauD•Fe(II)•αKG•taurine complexes of wild-type TauD and His99Ala-TauD; and tables comparing salient bond angles of the structures **1**−**17**. This material is available free of charge via the Internet at http://pubs.acs.org.

JA067899Q